

# Mutual Decoupling for Massive MIMO Antenna Arrays by Using Triple-Layer Meta-Surface

SHENGYUAN LUO<sup>1</sup>, YIMING ZHANG<sup>ID</sup><sup>2</sup> (Member, IEEE),  
GERT FRØLUND PEDERSEN<sup>ID</sup><sup>1</sup> (Senior Member, IEEE),  
AND SHUAI ZHANG<sup>ID</sup><sup>1</sup> (Senior Member, IEEE)

<sup>1</sup>Antenna, Propagation and Millimeter-Wave Systems Section, Aalborg University, 9220 Aalborg, Denmark

<sup>2</sup>Guangdong Provincial Key Laboratory of Optoelectronic Information Processing Chips and Systems, School of Electronics and Information Technology, Sun Yat-sen University, Guangzhou 510006, China

CORRESPONDING AUTHOR: S. ZHANG (e-mail: sz@es.aau.dk)

This work was supported by the China Scholarship Council (CSC).

**ABSTRACT** The high isolation massive antenna arrays are the key devices in the base station of the future wireless communication systems. The challenge for the array application is how to reduce the coupling among the array elements. This paper introduces a new decoupling method for massive MIMO arrays with an inner-element distance of around half wavelength by using a triple-layer metasurface (TMS). The TMS comprises three identical surfaces. The waves reflected from the bottom metasurface (MS) and top two-layer MS have the same amplitudes and the opposite phases, which are canceled with each other. An example of  $4 \times 4$  dual-polarized wideband microstrip array with a TMS is proposed to verify the decoupling method. The simulation and measurement show that the TMS can help reduce the coupling among the array elements to less than -24 dB in both the co-polarization and cross-polarization directions within 4.23-4.82 GHz. In the meanwhile, the radiation characteristics of the arrays with and without TMS are almost unchanged.

**INDEX TERMS** Decoupling, dual-polarized, massive multiple-input multiple-output (MIMO) antenna array, triple-layer metasurface (TMS), wideband.

## I. INTRODUCTION

THE FUTURE wireless communication technology boosts the development of wireless communication [1]. The multiple-input multiple-output (MIMO) has attracted much attention in recent years because it can significantly improve the data throughput and transmission distance without increasing its bandwidth or the total transmit power [2], [3]. The massive MIMO system, scales up from the MIMO system, has a higher transmission ratio, spectrum efficiency, and channel capacity [4], [5]. When a massive MIMO array with an inner-element distance around half wavelength is implemented, the mutual coupling is inevitable [6]. Recently, researchers found that the coupling of the arrays, basically consists of space wave coupling component, seriously deteriorate the antenna performance [7],

[8], [9], [10], [11], [12], [13], [14], [15], [16], [17]. Thus, low coupling of the massive MIMO array has become a crucial indicator during the implement.

Numerous decoupling techniques for MIMO arrays have been observed: mutual decoupling network [18], [19], defected ground structure [20], electromagnetic bandgap [21], metamaterial [22], parasitic decoupling technique [23], and energy cancellation [24]. In addition, the metasurface (MS) as an effective decoupling technology for arrays has been studied and reported in [25] and [26]. In [23], a suspended MS is placed above the array, where the surface is equivalent to a negative permeability medium to reject the propagation of the waves. However, it cannot be applied in dual-polarized antenna arrays because of its asymmetry. In [26], a novel MS employs a near-field resonator (NFR)

above each antenna element. However, it is not available to be scaled up to dual-polarized arrays because it will increase the coupling in the orthogonal modes.

Many decoupling methods for the massive MIMO arrays have been reported [27], [28], [29], [30], [31], [32]. A non-resonant metasurface (NMS) with a was proposed in [27] to suppress the propagation of the space waves. Here, a negative permeability and positive permittivity along the tangential direction of the array can be abstracted. A transmission-line-based decoupling method was proposed in [28], which enables well-cancels coupling for the adjacent elements but slightly drops the total efficiencies. Moreover, its relative working band is pretty narrow. Reference [29] introduced a decoupling ground (DG), which changes the ground current path to enable well-cancel with the space wave coupling. Yet, it needs a relatively sizeable inner-element distance to adjust the shape of the ground plane. A concept of array-antenna decoupling surface (ADS) for massive MIMO arrays was proposed [30]. But the arrays with ADS elements have complicated design procedures and relatively larger sizes. Additionally, a decoupling method of phase compensation based on the concept of ADS for large-scale staggered dual-polarized dipole arrays is further investigated to simultaneously reduce the couplings between adjacent co-polarized array elements with diversified phase laggings [31]. Yet, it has the same problem as the method mentioned in [30]. A new method of decoupling dielectric stubs (DDS) is proposed as perturbations to constrain the electromagnetic fields of the array element [32]. However, dielectric stubs with low permittivity are needed to reduce transmission loss.

In this paper, a triple-layer metasurface (TMS) concept is proposed and experimentally demonstrated. The TMS is composed of three identical MSs and placed above the arrays. Here, the waves reflected from the bottom layer MS and the top two-layer MS have the same amplitudes and opposite phases to enable perfect cancellation. Consequently, the coupling of the arrays can be significantly reduced by utilizing the proposed TMS. A factual example of a  $4 \times 4$  massive array is studied to verify the proposed decoupling method. The proposed TMS for massive MIMO arrays has some novelties as:

1. The coupling of the massive MIMO arrays with the inner-element distance of around half-wavelength mainly results from the space waves coupling component. For this, the method TMS develops two paths for the space waves coupling component, which has a phase difference of  $180^\circ$  and an amplitude difference of 0 to obtain well cancellation.

2. The proposed TMS features symmetry in orthogonal directions that can be utilized in dual-polarized arrays. At the same time, it has a stable radiation performance over the wide working band of the arrays.

3. The arrays with the TMS have a low loss. Moreover, it can be implemented easily by adjusting the radius of the TMS element and the thickness of the air gaps between TMS.

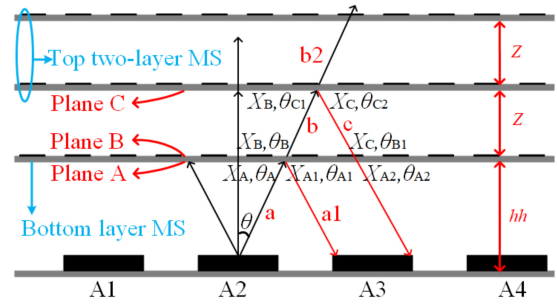


FIGURE 1. The decoupling schematics of the TMS.

This paper is organized as follows: in Section II, the concept of the TMS method is carefully described, and then a TMS unit is designed and analyzed. The decoupling method TMS for massive MIMO array is applied in Section III. First, a dual-polarized and wideband microstrip array is proposed. Then, the TMS is placed above the reference array. Finally, the simulated and measured results are presented to verify the proposed decoupling method. Section IV concludes the paper.

## II. PROPOSED DECOUPLING TECHNIQUE

### A. CONCEPT OF THE PROPOSED TMS MUTUAL DECOUPLING METHOD

Figure 1 gives the theoretical analysis of the decoupling mechanism of the TMS for the massive MIMO arrays. The key to the decoupling for the space coupling is introducing two kinds of reflection waves with the same amplitudes and opposite phases. The reflection waves can be divided into two parts: the waves reflected from the bottom MS and the waves reflected from the top stack MS. The top stack MS can be seen as an amplitude and phase shifter, enabling the reflection waves to have the same amplitudes and opposite phase as the waves reflected from the bottom MS. It is worth noting that the second kind of reflection wave is introduced based on the waves passed from the bottom MS. Therefore, the top stack MS must have a high reflection coefficient. In this paper, a non-resonant MS, which has a bandpass characteristic, is proposed to introduce partial reflection waves. Meanwhile, the rest partial space coupling component can propagate normally through the MS. Then, the top stack MS, composed of two layers of MS, has identical dimensions to the bottom-layer MS to get a high reflection coefficient. Finally, by appropriately adjusting the distance between three layers of metasurfaces, two kinds of waves reflected from the bottom layer MS and the top two-layer MS with opposite phases can be obtained. Consequently, a suppression for the space coupling can be obtained. When the TMS is suspended above the array, the waves reflected from the bottom layer MS and the top two-layer MS have the same amplitudes and opposite phases, which can be cancelled by appropriately adjusting the size of the TMS. As shown in Figure 1, the bottom surface and the top surface of the bottom layer MS are defined as Plane A and Plane B, respectively. The

phase of the space coupling component  $a$  on plane A is marked as  $\theta_A$ . In the meanwhile, the phase of the reflection component  $a_1$  on plane A can be expressed as:

$$\theta_{A1} = \theta_A + \theta_{\text{ref1}} \quad (1)$$

where the  $\theta_{\text{ref1}}$  is the phase of the reflection coefficient of the bottom layer MS. When the waves propagate through the bottom MS, it will introduce a transmitted phase delay  $\theta_{\text{tra1}}$ . The phase of the transmitted wave  $b$  on Plane B can be calculated as:

$$\theta_B = \theta_A + \theta_{\text{tra1}} \quad (2)$$

When the transmitted component  $b$  propagates to plane C, it will have a phase delay that can be expressed as:

$$\theta_{\text{delay}} = (Z/\lambda) \times 360^\circ \quad (3)$$

The phase  $\theta_{C1}$  of the waves on plane C can be calculated as:

$$\theta_{C1} = \theta_A + \theta_{\text{tra1}} + \theta_{\text{delay}} \quad (4)$$

The phase of the reflected waves on plane C can be calculated as:

$$\theta_{C2} = \theta_{C1} + \theta_{\text{ref2}} \quad (5)$$

$$\theta_{C2} = \theta_A + \theta_{\text{tra1}} + \theta_{\text{delay}} + \theta_{\text{ref2}} \quad (6)$$

Here, the  $\theta_{\text{ref2}}$  represents the phase of the simulated S11 of the top two-layer MS. When the waves reflect from Plane C propagate to the bottom layer MS, there will be a phase delay too. Therefore, the phase of the reflected waves on plane B can be expressed as:

$$\theta_{B1} = \theta_{C2} + \theta_{\text{delay}} \quad (7)$$

$$\theta_{C1} = \theta_A + \theta_{\text{tra1}} + \theta_{\text{delay}} \times 2 + \theta_{\text{ref2}} \quad (8)$$

Furthermore, the phase of the waves on plane A reflected from plane C can be calculated as:

$$\theta_{A2} = \theta_A + \theta_{\text{tra1}} \times 2 + \theta_{\text{delay}} \times 2 + \theta_{\text{ref2}} \quad (9)$$

Since the waves reflected from plane A and plane C have the same amplitudes and the opposite phase. Therefore the  $\theta_{A2}$  can also be expressed as:

$$\theta_{A2} = \theta_{A1} + 180^\circ \quad (10)$$

$$180^\circ = \theta_{\text{tra1}} \times 2 + \theta_{\text{delay}} \times 2 + \theta_{\text{ref2}} \quad (11)$$

$$\theta_{\text{delay}} = \left(180^\circ - \theta_{\text{tra1}} \times 2 - \theta_{\text{ref2}}\right)/2 \quad (12)$$

The thickness of the air gap  $Z$  between the MSs can be calculated as:

$$Z = \left(\left(\left(180^\circ - \theta_{\text{tra1}} \times 2 - \theta_{\text{ref2}}\right)/2\right)/360\right) \times \lambda \quad (13)$$

The phase difference  $\theta_{\text{dif}}$  between  $\theta_{A1}$  and  $\theta_{A2}$  can be expressed as:

$$\theta_{\text{dif}} = \theta_{\text{tra1}} \times 2 + \theta_{\text{delay}} \times 2 + \theta_{\text{ref2}} - \theta_{\text{ref1}} \quad (14)$$

Regarding for the amplitudes, the amplitudes of the reflection coefficient and the transmission coefficient of the bottom

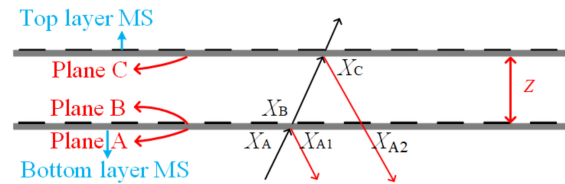


FIGURE 2. The phase distribution of the space waves on two-layer MS.

layer MS can be defined as:  $R_1$  and  $T_1$ , respectively. Meanwhile, the amplitude of the reflection coefficient of the top two-layer MS can be marked as:  $R_2$ . When the amplitude of the coupling component is  $X_A$ , the amplitude of the waves reflected from the bottom layer MS is  $X_{A1}$ , and the amplitude of the transmitted waves from the bottom layer MS is  $X_B$ . And then, the amplitude of the waves reflected from the top two-layer MS on plane C is  $X_C$ , while the amplitude of the waves reflected from the top two-layer MS on Plane A is  $X_{A2}$ .

$$X_{A1} = X_A \cdot R_1 \quad (15)$$

$$X_B = X_A \cdot T_1 \quad (16)$$

$$X_C = X_B \cdot R_2 \quad (17)$$

$$X_C = X_A \cdot T_1 \cdot R_2 \quad (18)$$

$$X_{A2} = X_C \cdot T_1 \quad (19)$$

$$X_{A2} = X_A \cdot T_1^2 \cdot R_2 \quad (20)$$

The Amplitude difference between the waves reflected from the bottom layer MS and the one reflected from the top two-layer MS on plane A can be calculated as:

$$X_{\text{dif}} = X_{A1} - X_{A2} \quad (21)$$

$$X_{\text{dif}} = X_A \cdot \left(R_1 - T_1^2 \cdot R_2\right) \quad (22)$$

According to the analysis for the decoupling mechanism of TMS, the amplitude calculated difference equal to 0 from the formula (22).

In addition, it is needed to analyze why the two-layer MS cannot be used to reduce the coupling of the arrays, where the two MSs has same dimensions. Resemble to Figure 1, a two-layer MS placed above the reference array with corresponding phase distribution is shown in Figure 2. The amplitude of waves reflected from the top layer MS on plane C can be presented as:

$$X_C = X_A \cdot T_1 \cdot R_2 \quad (23)$$

Furthermore, the wave reflected from the top layer MS on plane A can be expressed as:

$$X_{A2} = X_A \cdot T_1^2 \cdot R_2 \quad (24)$$

Therefore, the amplitude of the two kinds reflected waves can be calculated as:

$$X_{\text{dif}} = X_A \cdot \left(R_1 - T_1^2 \cdot R_2\right) \quad (25)$$

The calculated results reveals that the amplitude difference does not equal to 0, which demonstrate that the two-layer MS cannot be used to suppress the coupling of the arrays.

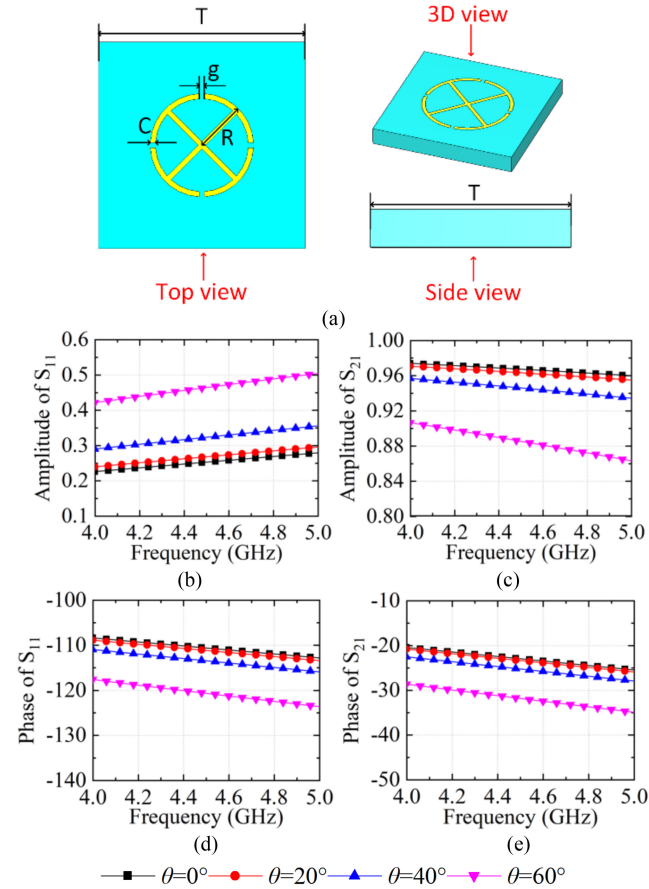


**FIGURE 3.** Detail structure, the amplitudes, and the phases of the S-Parameters of the bottom layer MS with different incident angle  $\theta$ : (a) the bottom-layer MS, (b) the amplitude of the  $S_{11}$ , (c) the amplitude of the  $S_{21}$ , (d) the phase of the  $S_{11}$ , (e) the phase of the  $S_{21}$ .

Therefore, A TMS is adopted to reduce the mutual coupling of the massive MIMO antenna arrays.

### B. DESIGN OF THE TMS

The periodic unit with a feature of symmetry along  $x$ -axis and  $y$ -axis is designed to meet the requirement for the decoupling of the wideband and dual-polarization massive MIMO arrays. A circular and cross-shaped patches are integrated into the same MS unit with four splits in the  $x$ -direction and the  $y$ -direction. The metal patch of the MS element is printed on a Rogers RO4350B substrate with a thickness of 1.52mm, a relative permittivity of 3.66 and a loss tangent of 0.0037. The bottom layer MS element is depicted in Figure 3 (a) from the top view, front view, and perspective view, respectively. For a uniform surface, the size of the MS element must be smaller than a certain value. It is worth noting that the size of the MS element cannot be too small because it will make it difficult to optimize the MS dimensions. A compromise scheme is adopted, where  $5 \times 5$  MS elements are arranged above the array element, and the length of the MS element is set as 8 mm. To guarantee the waves radiated from the array can propagate normally into space, a non-resonant MS unit is adopted that performs bandpass characteristics. Thus, the gap between the metal patches in

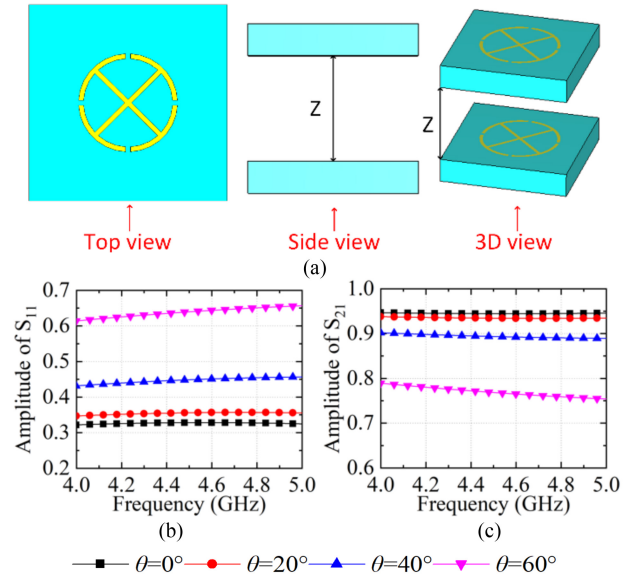


**FIGURE 4.** Detail structure of the top two-layer MS, the amplitudes, and the phases of the S-Parameters of the top two-layer MS with different incident angle  $\theta$ : (a) the top two-layer MS, (b) the amplitude of the  $S_{11}$ , (c) the phase of the  $S_{11}$ .

the adjacent MS unit must be big enough, which means the patch cannot completely fill the substrate surface of the MS element. In Addition, a partial space coupling component can be reflected by the MS. Correspondingly, the radius of the circle patch of the MS element is set as 2 mm. The split on the circle patch is used to increase the electro length in a limited space. Enhance, the width of the entire TMS is set as 0.2 mm. The air gap is mainly used to adjust the phase of the waves reflected from the top two-layer. After calculating according to the formula (13), the  $Z$  is set as 5 mm. A comprise scheme of a triple-layer metasurface (TMS) is adopted to avoid the problem of the high profile of the array. For the factual massive MIMO arrays, the space coupling component is radiated to the MS with an incident angle  $\theta$  along the normal direction of the arrays. Therefore, the transmission coefficient and the phase of the S-parameters with various incident angles of  $\theta$  are studied and shown in Figure 3. Generally, the energy radiated from the microstrip focus within the angular range of  $-60^\circ$  to  $60^\circ$ , which means when the incident angle is larger than  $60^\circ$ , the space coupling component is weak enough and can be ignored. At the same time, it is hard for the massive MIMO array to scan over  $\pm 60^\circ$ . For the reason that the incident angle is fixed from  $0^\circ$  to  $60^\circ$ . Figure 3 (b) and Figure 3 (c) show that when the  $\theta$  varies from  $0^\circ$  to  $60^\circ$  with a step of  $20^\circ$ , the transmission loss of the bottom layer MS increases yet still shows a high transmission performance over the operating band. Figure 3 (d) and Figure 3 (e) depict that the phase of the  $S_{11}$  and  $S_{21}$  slightly increases as the  $\theta$  varies from  $0^\circ$  to  $60^\circ$ . Moreover, when the  $\theta$  is  $0^\circ$ , the phase of the  $S_{11}$  and  $S_{21}$  is  $-115^\circ$  and  $-30^\circ$ , respectively. Figure 3 also reveals that the bottom layer MS exhibits a stable transmission and reflection characteristic within a wide working band.



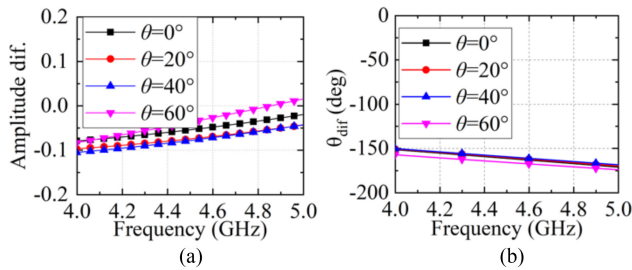


**FIGURE 5.** The calculated amplitude difference  $A_{dif}$  and phase difference between the waves reflected from the bottom-layer MS the top two-layer MS when the incident angle of  $\theta$  varies from  $0^\circ$  to  $60^\circ$  with the step of  $20^\circ$ : (a) amplitude difference, (b) phase difference.

Figure 4 shows the two-layer MS structure from front, top, the perspective views, and the corresponding S-parameters. The top two-layer MS has the same sizes as the bottom layer MS. Figure 4 (a) shows the detailed structure of the two-layer MS. Figure 4 (b) depicts that with the increase of the  $\theta$ , the reflection increases too, but the transmission decreases. Figure 4 (c) demonstrates that the phase of the S-parameters of the two-layer MS almost has no change with different  $\theta$ .

Based on the theoretical analysis of the decoupling mechanism of TMS for the massive MIMO arrays (see in Figure 1), the amplitude difference  $X_{dif}$  and the phase difference  $\theta_{dif}$  between the waves reflected from the bottom layer MS and top two-layer MS are calculated and given in Figure 5 by varying the incident angle of  $\theta$  from  $0^\circ$  to  $60^\circ$  with the step of  $20^\circ$ . The calculated results demonstrate that the amplitude and phase differences between the waves reflected from the bottom layer MS and top two-layer MS basically equal to 0 and  $180^\circ$ , respectively. The calculated results justify that these two kinds of waves can be canceled with each other.

The simulation results in Figure 3 and Figure 4 demonstrate that the amplitudes and phases keep calm and range within a small scale within a bandwidth of 4.0 - 5.0 GHz. The amplitude differences in Figure 5 range from  $-0.1$  to  $0.02$  within the entire simulation band. At the same time, the phase differences are close to  $180^\circ$ . It repeats that the decoupling method of TMS owes a wideband performance from 4.0 to 5.0 GHz, and the decoupling band of the massive MIMO array depends on the working band of the original array. It can obtain a wider decoupling band by optimizing or redesigning the structure of the array element.

According to the simulated results and the analysis of the decoupling method of the TMS, the waves reflected from the bottom two-layer MS and the top layer MS are out of phase and can be cancelled with each other too. The redundant description will not be done due to the limitation of the page.

**C. SIMULATIONS FOR THE VERIFICATION OF THE PROPOSED DECOUPLING METHOD**

In this subsection, we take a dual-polarization two-element array shown in Figure 6 as an example to study the

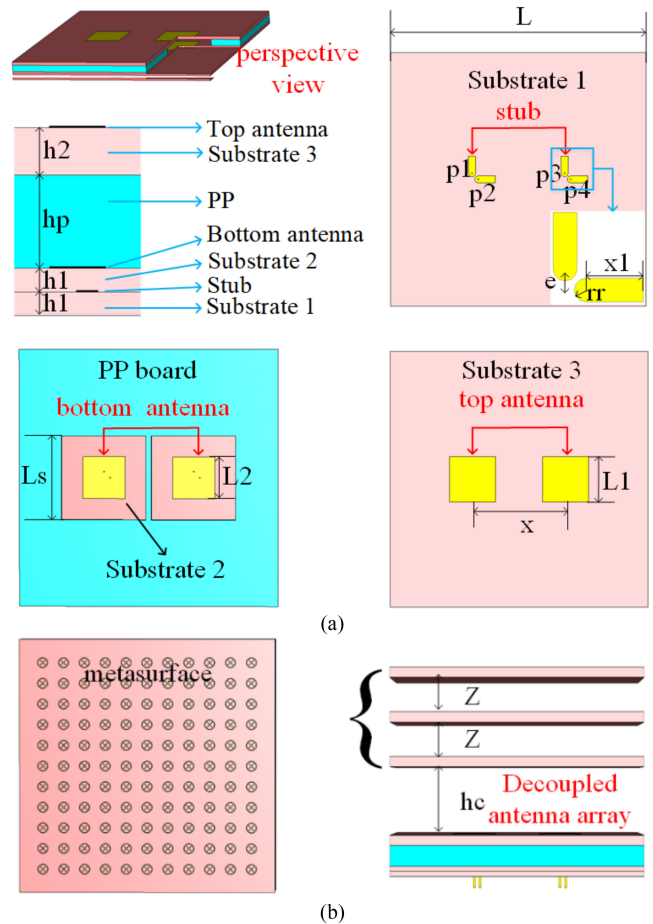


**FIGURE 6.** The structure of the antenna array with and without TMS: (a) the overall structure of the reference array with specific dimensions, (b) the detailed structure of the array with TMS.

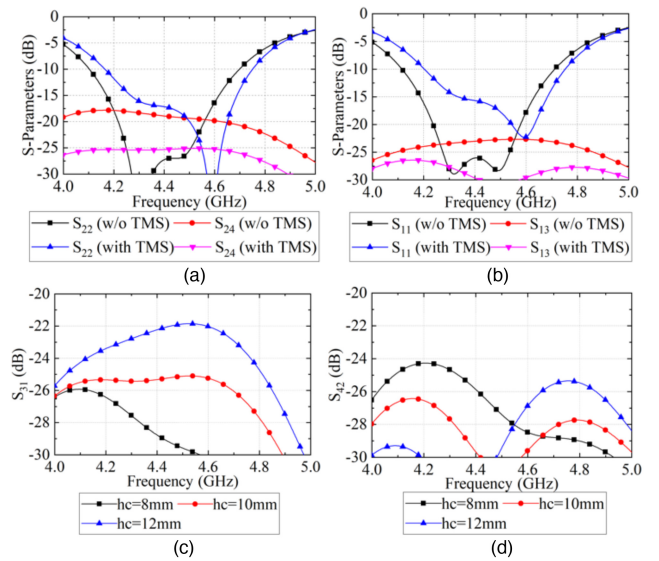
decoupling mechanism of the TMS. The detailed dimensions of the array are shown in the figures as well. The wide-band dual-polarization array is composed of two layers of patch antennas. The top antenna is placed above the bottom one and supported by a PP (polypropylene) board with a dielectric constant of 2.2. The two patch antenna elements are printed on a Rogers RO4350B substrate with a relative permittivity of 3.66 and a loss tangent of 0.0037. The bottom patch antenna consists of two substrates with the same thickness of 0.762 mm, and the thickness of the substrate of the top antenna is 1.524 mm. The array is fed with coaxial cables. The feed points of the array elements are set in the x-axis and y-axis directions to achieve dual-polarization. The metal stubs are printed on the bottom surface of substrate 2, as shown in Figure 6 (a), and connect with the bottom antennas by drilling metal vias. After the inner connectors of the coaxial cables are connected to the bottom antennas, the metal stubs are automatically connected to the inner connector. By adjusting the length of the metal stubs, the best impedance matching of the antennas can be obtained. Two cavities are engraved on the PP board directly above the bottom antenna to provide a space for PCB solder. This

**TABLE 1.** Parameters of the TMS.

parameters	$L$	$X$	$X1$	$rr$	$L1$	$Ls$	$L2$
Value(mm)	98	33	6.2	1.3	16	31	16.8
parameters	$h1$	$hp$	$h2$	$hc$	$Z$	$T$	$g$
Value(mm)	0.762	3	1.524	10	5	8	0.2
parameters	$C$	$R$	$e$				
Value(mm)	0.2	2	2.3				

kind of antenna must consist of two layers of substrates to arrange the metal stubs increasing the complexity of the fabrication. Generally, the substrates in mm-wave antennas should be compact as possible. Although the air gap is extremely tiny from a macro perspective, its thickness cannot be ignored relative to the wavelength of the mm-wave antenna. Consequently, this antenna cannot be extended to the mm-wave antenna. The feature of wideband of the massive MIMO array in this paper was carried out by introducing two resonant modes, where the top and bottom antennas correspond to high and low resonant frequencies, respectively. Correspondingly, the top antenna is smaller than the bottom antenna, and they have sizes of 16 mm and 16.8 mm, respectively. The pp board only supports the upper antenna so that the sizes of the air cavities should be as large as possible, or it will affect the effective dielectric constant of the substrate of the top antenna. According to this, the sizes of the air cavities are set as 31 mm, which is only 2mm smaller than the half wavelength of the antenna. It is worth noting that the thickness of the PP board is a crucial parameter in the design procedure of the antenna. If the PP board is too thinner, the two resonant frequencies of the wideband antenna will not be close together, eventually forming a dual-band antenna. However, if it is too thicker, the two resonant frequencies will overlap, and the bandwidth of the antenna cannot be extended. Therefore, a compromising means is applied, and the thickness of the PP board is set as 3 mm. At the same time, the inter-element distance is a half wavelength. Table 1 gives the detailed dimensions of the antenna array with and without TMS.

Figure 7 (a) and (b) show the S-parameters of the arrays in the x-polarization and y-polarization. It demonstrates that by using the TMS, the couplings of the array in x-polarization and y-polarization are reduced to  $-25$  dB and  $-26.4$  dB over the working band. The operating band of the decoupled array in dual-polarization is 4.2-4.75 GHz. Moreover, the operating band of the array shifts to a higher band slightly. Initially, the distance  $hc$  between the array and TMS determines the decoupling level. The S-parameters of the decoupled array with different  $hc$  are presented in Figure 7 (c) and Figure 7 (d). It demonstrates that when the  $hc$  is 10 mm, the envelope of the  $S_{31}$  and  $S_{42}$  in dual-polarization is the lowest. This example perfectly verifies the proposed decoupling method TMS for the MIMO arrays.


**FIGURE 7.** The S-parameters of the arrays: (a) the S-parameters of the array with and without TMS in x-polarization, (b) the S-parameters of the array with and without TMS in y-polarization, (c) the  $S_{31}$  of the decoupled array with different  $hc$ , (d) the  $S_{42}$  of the decoupled array with different  $hc$ .

### III. DESIGN EXAMPLE

For the dual-polarized massive MIMO arrays, the paths of the space waves coupling in dual-polarization and diagonal directions are complicated. Thus, the coupling between the adjacent and nonadjacent array elements is hardly reduced to the lowest level simultaneously. Therefore, the envelope of the S-parameters of all the paths should be lower than  $-24$  dB.

#### A. ANTENNA CONFIGURATION OF $4 \times 4$ ARRAY

A  $4 \times 4$  dual-polarization massive MIMO array with TMS is carried out to verify the proposed decoupling method TMS. Figure 8 illustrates the configurations of the array with the specific dimensions and the corresponding prototype. The  $4 \times 4$  array adopts the same antenna element mentioned in previous mentioned one. The TMS is mounted above the array, and a prototype has been fabricated and installed. The antennas and TMS are fixed together with nylon screws. The substrates have non-metalized holes at the corners to provide space for nylon screws to pass through. A foam board is placed directly above the array to support the TMS. The  $4 \times 4$  array with TMS and the corresponding fabricated prototype are shown in Figure 8 (a) and (b), respectively.

#### B. ANTENNA PERFORMANCE

The S-parameters of the  $4 \times 4$  arrays with and without TMS are simulated. And then, those of the array with TMS are measured. The results are shown in Figure 9. Since the antenna array is symmetrical along x-direction and y-direction, the S-parameters of port 12 in the second quadrant are chosen and displayed. The couplings mainly exist among neighbouring and non-neighbouring elements in the x-direction, y-direction, and diagonal directions

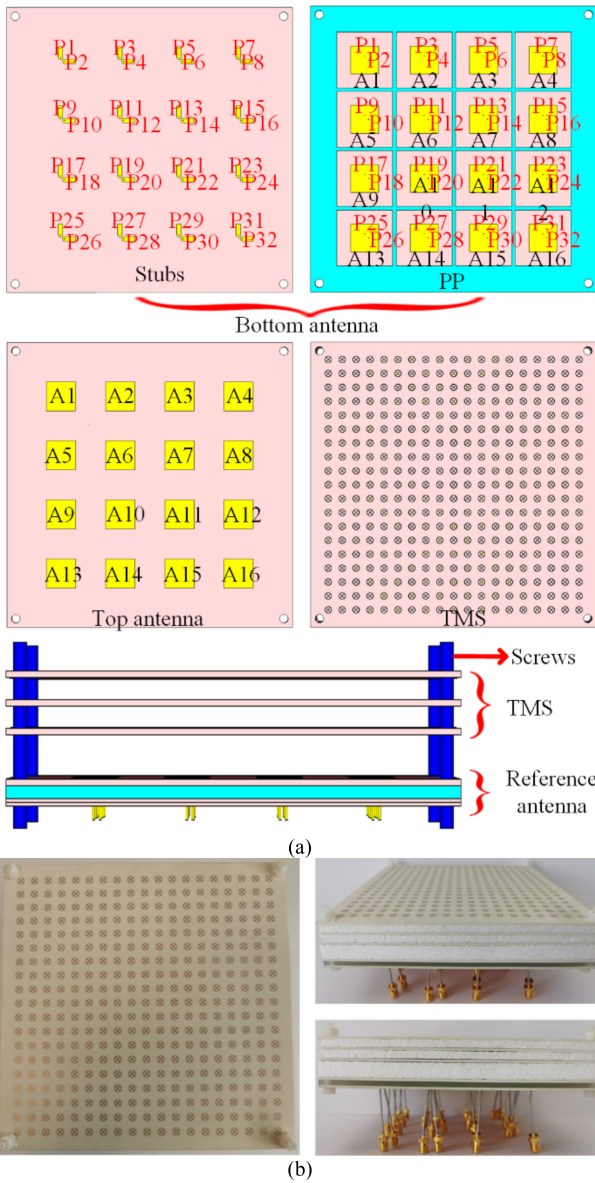


**FIGURE 8.** The structure of the  $4 \times 4$  array with and without TMS: (a) the detailed structure of the array with TMS from top and side views, (b) the fabricated prototype of the array with TMS from the top, side and perspective views.

of the massive MIMO array. The  $S_{2,12}$  refers to the coupling between the adjacent elements in the diagonal direction of the array. The  $S_{4,12}$ ,  $S_{10,12}$ ,  $S_{16,12}$  and  $S_{28,12}$  represent the couplings between the neighbouring and non-neighbouring elements in y-polarization and x-polarization, respectively. For the measurement of the S-parameter, we use the PNA Network Analyzer N5227B (10 MHz – 67 GHz). After the calibration step is carried out automatically, the S-parameters are measured. The simulation results show that the proposed array with TMS works from 4.217–4.763 GHz, and all the port-to-port isolation can be improved from 17 dB to over 24 dB within the whole operating band. The impedance matching bandwidth of the array has a slight shift to the higher band. The measured results show that the

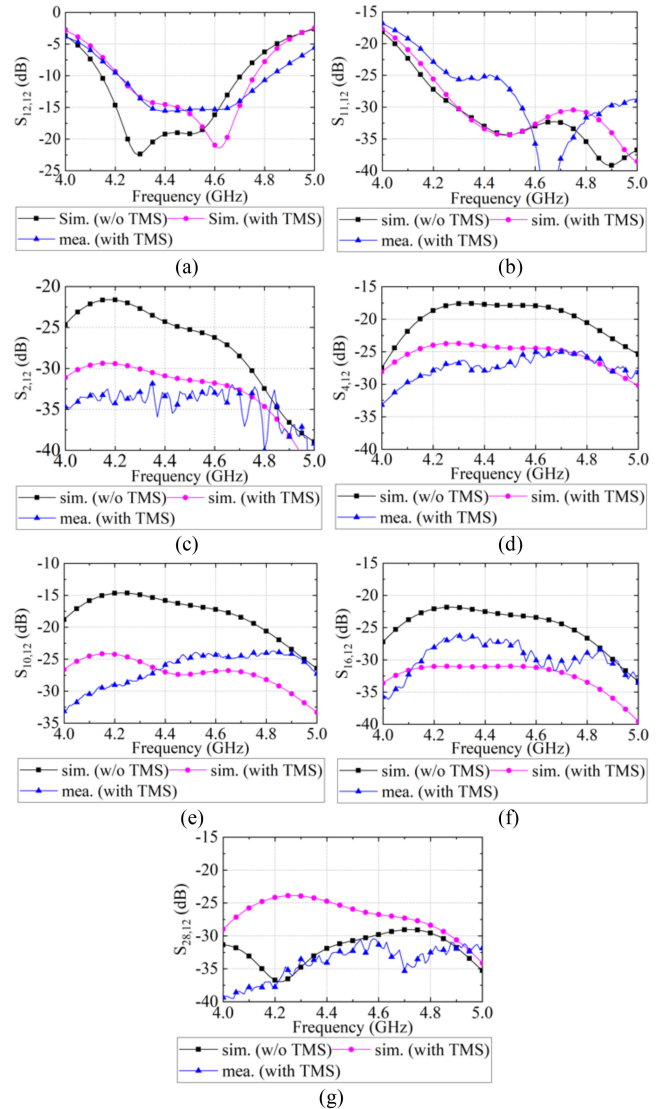


**FIGURE 9.** The simulated and measured S parameters of the  $4 \times 4$  array with/without TMS: (a)  $S_{12,12}$ , (b)  $S_{11,12}$ , (c)  $S_{2,12}$ , (d)  $S_{4,12}$ , (e)  $S_{10,12}$ , (f)  $S_{16,12}$  and (g)  $S_{28,12}$ .

operating band of the array is 4.23–4.82 GHz. The difference between the simulated and measured working band of the array is caused by the fabrication mistake. Due to the page length limitation, the rest S-parameters are not shown.

The element A12 have all types of coupling paths because of the features of symmetry, and it has similar radiation patterns with rest elements. The radiation patterns of antenna A12 at 4.5, 4.6, 4.7, and 4.8 GHz are selected. The measurement for the radiation performance of the  $4 \times 4$  array is carried out in a SATIMO SG24L chamber, which can provide an interference-free environment for the radiation patterns measurement. During the measurement, a horn antenna is utilized for the calibration. When we measure the radiation patterns of the array, the P12 (see Figure 7(a)) is fed, and the other ports connect with 50-ohm loads. The microwave chamber can provide an interference-free environment for the radiation patterns measurement. The radiation



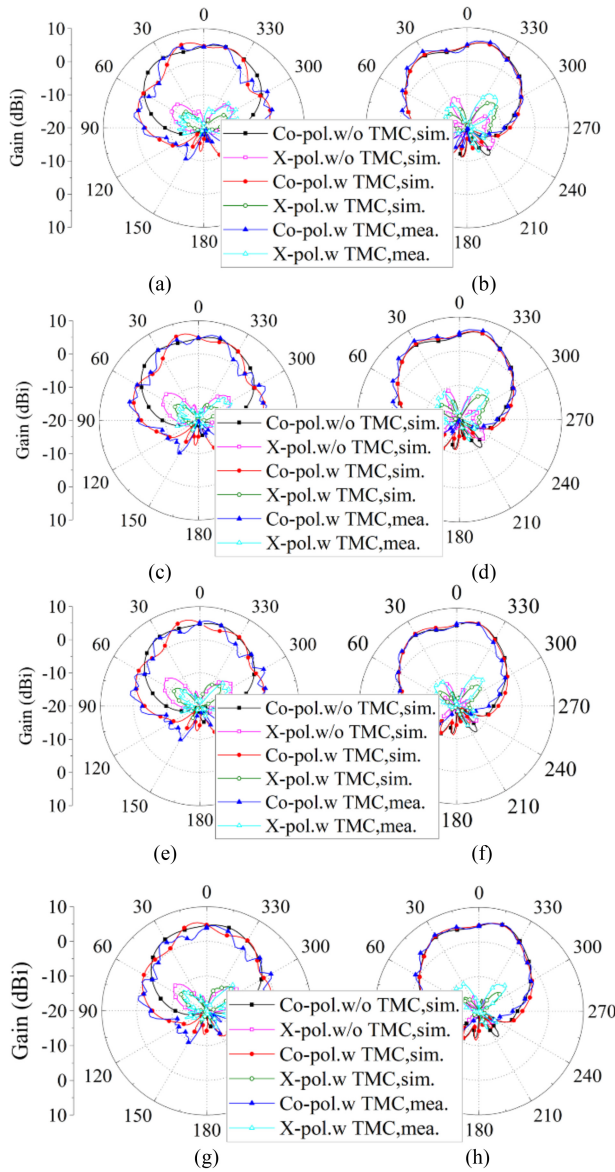


**FIGURE 10.** The radiation patterns of the array with and without TMS, (a) E-plane of port 12 at 4.5GHz, (b) H-plane of port 12 at 4.5GHz, (c) E-plane of port 12 at 4.6GHz, (d) H-plane of port 12 at 4.6GHz, (e) E-plane of port 12 at 4.7GHz, (f) H-plane of port 12 at 4.7GHz, (g) E-plane of port 12 at 4.8GHz, (h) H-plane of port 12 at 4.9GHz.

patterns of the array without and without the TMS are shown in Figure 10. The measured results show a slight drop in E-plane compared with the simulated one. The tolerance mainly comes from four aspects: the power loss in the substrate, the soldering part, the measurement process, and fabrication mistake. Since the substrates have a loss tangent of 0.0037, the power loss in the substrate is fragile. Instead, the soldering parts between feeding ports and coaxial cables, which do not exist in the simulation model, introduce power loss that leads to measurement tolerance. During the measurement process, the cable lines connecting to the array also bring the power loss, which generates measurement error. In addition, the fabrication error introduces measurement tolerance, too. But the contours of the patterns are almost same. The measured

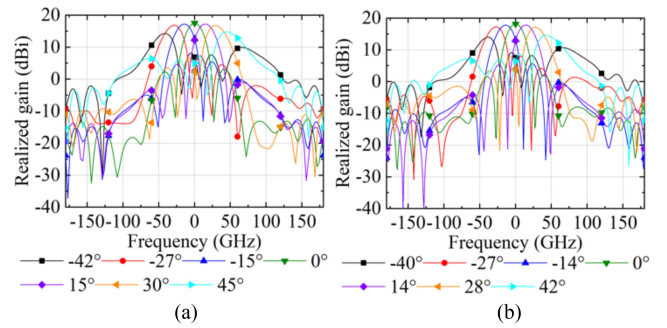


**FIGURE 11.** The beam scanning of the array with/without TMS: (a) without TMS, (b) with TMS.

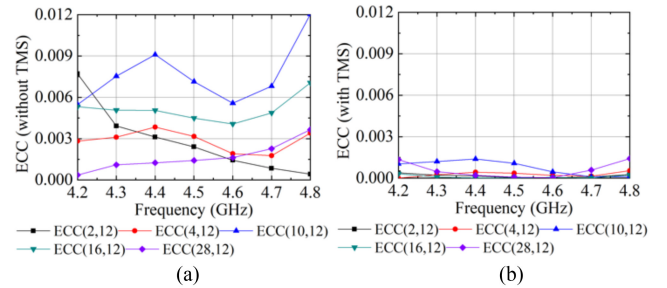


**FIGURE 12.** ECC of the array with/without TMS: (a) without TMS, (b) with TMS.

patterns of the decoupled array in the H-plane match well with the simulated results before adding TMS. The results show that the radiation patterns of the array with and without loading TMS almost keep consistent. The radiation patterns of other array elements are measured and have similar results with the A12, which are not shown due to the page limitation. It aligned well with the theoretical analysis.

The beam scanings of the  $4 \times 4$  array with and without the TMS are given in Figure 11 (a) and (b), respectively. It clears that after applying the TMS, the beam scanning capability is reduced from  $-42^\circ - 45^\circ$  to  $-40^\circ - 42^\circ$ .

The Envelop Correlation Coefficient (ECC) represents the correlation between the received signal amplitudes between different antenna elements. It is a key indicator to measure the diversity performance and coupling performance of the MIMO system. The ECC can be calculated from the formula (26) and shown as follows. As the prementioned theoretical analysis, the ECCs between port 12 and ports 2, 4, 10, and 16 can present all the types. The corresponding calculated ECCs for the  $4 \times 4$  dual-polarization massive MIMO array with and without TMS are presented in Figure 12 (a) and Figure 12 (b), respectively. After introducing the TMS, the ECCs have been reduced from 0.012 to 0.0015, which leads to a poor correlation between the array elements.

$$\rho_e = \frac{\left| \int \int_{4\pi} \left[ \vec{E}_1(\theta, \phi) \cdot \vec{E}_2(\theta, \phi) \right] d\Omega \right|^2}{\int \int_{4\pi} \left| \vec{E}_1(\theta, \phi) \right|^2 d\Omega \cdot \int \int_{4\pi} \left| \vec{E}_2(\theta, \phi) \right|^2 d\Omega} \quad (26)$$



TABLE 2. Parameters comparison.

Ref.	[28]	[29]	[30]		[31]		[32]	This work
Decou. method	Transmission line	DG	ADS		ADS		DDS	TMS
Antenna type	Mic. Ant.	Mic. Ant.	Mic. Ant.	Mon.	Sta. Dip.	Sta. Dip.	Mic. Ant.	Mic. Ant.
Polarization	Dua.-pol.	Dua.-pol.	Sin.-pol.	Dua.-pol.	Dua.-pol.	Dua.-pol.	Dua.-pol.	Dua.-pol.
Array configuration	2 × 2	4 × 4	1 × 8	2 × 2	4-4-4-4	2-1-2	4 × 4	4 × 4
Freq. (GHz)	2.395-2.52	4.9-5.2	2.4-2.5	3.3-3.8	3.3-3.8	3.3-3.75	4.4-5.0	4.23-4.82
Height ( $\lambda_0$ )	NA	0.25 $\lambda_0$	0.318 $\lambda_0$	0.33 $\lambda_0$	0.4 $\lambda_0$	0.39 $\lambda_0$	0.466 $\lambda_0$	0.45 $\lambda_0$
Antennas distance ( $\lambda_0$ )	0.5 $\lambda_0$	0.62 $\lambda_0$	0.45 $\lambda_0$	0.71 $\lambda_0$	0.5 $\lambda_0$	0.4 $\lambda_0$	0.485 $\lambda_0$	0.5 $\lambda_0$
Isolation	25	24.5	24	25	25	25	25	24
Compl. of the decoupling structure	complicated	complicated	complicated		complicated		simple	simple
Subs. of decoupling structure	Rogers RO3003 ( $\epsilon_r = 3$ )	Rogers RO4350B ( $\epsilon_r = 3.66$ )	NA ( $\epsilon_r = 2.6$ )		NA ( $\epsilon_r = 3$ )	Rogers Ro4730JXR ( $\epsilon_r = 2.98$ )	Poly lactide (PLA) ( $\epsilon_r = 2.65$ )	Rogers RO4350B ( $\epsilon_r = 3.66$ )
Effec. for massive MIMO ant. array	yes	yes	yes	yes	yes	yes	yes	yes

Mic. Ant.: Microstrip Antenna; Mon.: Monopole; Sta. Dip.: Staggered Dipole; Dua.-pol.: dual-polarization; Compl.: Complexity; Subs.: Substrate; Effec.: Efficiency.

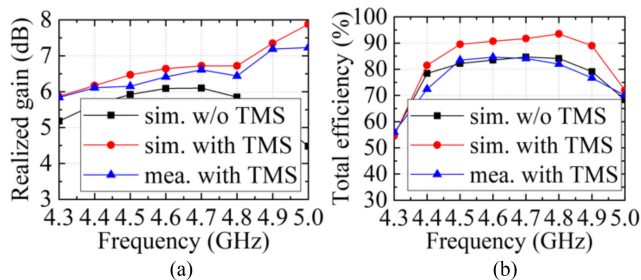


FIGURE 13. The Realized gain and efficiency of the array with TMS: (a) realized gain, (b) total efficiency.

The realized gain and the total efficiency of the element P12 at different frequencies before and after applying TMS are depicted in Figure 13 (a) and (b), respectively. The results in Figure 13 (a) show that the TMS improves the realized gain of the array. Meanwhile, Figure 13 (b) exhibits the array efficiency is more than 76%. Due to the fabrication accuracy error and the power loss in coaxial cables, the measured real gain and total efficiency drop slightly.

The proposed method of using TMS to reduce the coupling of massive MIMO antennas is universally applicable for the other frequency arrays. For the low-frequency arrays, it only needs to scale the sizes of the antenna proposed in this paper according to the corresponding ratio. Moreover, the relative bandwidth of the array will basically keep unchanged. However, for the mm-wave array, it is necessary to replace the basic array element, and the relative bandwidth of the decoupled array depends on the basic array element type.

It should be noted that the proposed decoupling method is difficult to be applied in dense mm-wave arrays because it does not have enough place to solder the feeding connectors.

#### IV. PERFORMANCE COMPARISON

An overall comparison between the proposed array with TMS and the other relevant techniques reported in recent literature is presented in Table 2. The decoupling performance for the massive MIMO array in this work is comparable with the one in the recent work. But this work exhibits superiority over the working band compared with the techniques in [28]. The array with DG in [29] has a working band from 4.9-5.2 GHz (at the center frequency of 4.9 GHz), which is relatively narrow. Meanwhile, the inner-element distance of the array is larger than 0.5 $\lambda_0$ . The ADS proposed in [30], [31] develops complicated space waves paths to suppress the coupling of the array. Therefore, it increases the design complexity of the ADS. The array with TMS in this work has a lower profile than the array proposed in [32]. In addition, a low dielectric constant of the DDS is needed because a higher dielectric constant negatively deteriorates the impedance match of the antenna element. In contrast, the TMS in our work has no specific requirements on the dielectric constant of the dielectric substrate. It demonstrates that the decoupling method TMS for massive MIMO array offers numerous merits over other mentioned decoupling techniques.

#### V. CONCLUSION

In this paper, a decoupling concept of the TMS was introduced. Then the decoupling mechanism of the TMS has

been thoroughly analyzed. A massive MIMO array consists of  $4 \times 4$  elements has been designed, simulated, fabricated. The simulated and measured results show that the coupling of the array has been reduced from -18 dB to -24 dB by using TMS. In contrast, the radiation performance of the array keeps unchanged. The measurements of the practical array by employing the TMS justify the feasibility of the proposed decoupling technique. Since the proposed TMS has simple structure and symmetry characteristics, it can be easily integrated with the massive MIMO array. Finally, the worst isolation of the antenna array can be obtained. Owing to the features of compact size, high isolation et al., the massive MIMO array integrated with the proposed TMS can be applied to satellite communication, fifth generation (5G) communication systems, Synthetic Aperture Radars (SAR), and so on.

## REFERENCES

- [1] I. Akyildiz, A. Kak, and S. Nie, "6G and beyond: The future of wireless communications systems," *IEEE Access*, vol. 8, pp. 133995–134030, 2020.
- [2] R. He, B. Ai, G. L. Stüber, G. Wang, and Z. Zhong, "Geometrical based modeling for millimeter wave MIMO mobile-to-mobile channels," *IEEE Trans. Veh. Technol.*, vol. 67, no. 4, pp. 2828–2863, Apr. 2018.
- [3] C. Li, H. Zhu, J. Cai, J. Hu, and G. Li, "Capacity analysis of terrestrial antenna array in distributed satellite MIMO communication system," *IEEE Trans. Veh. Technol.*, vol. 70, no. 5, pp. 4435–4450, May 2021.
- [4] Y. Liu, C.-X. Wang, J. Huang, J. Sun, and W. Zhang, "Novel 3-D non-stationary mmWave massive MIMO channel models for 5G high-speed train wireless communications," *IEEE Trans. Veh. Technol.*, vol. 68, no. 3, pp. 2077–2086, Mar. 2019.
- [5] H. Gao, Y. Su, S. Zhang, Y. Hou, and M. Jo, "Joint antenna selection and power allocation for secure co-time co-frequency full-duplex massive MIMO systems," *IEEE Trans. Veh. Technol.*, vol. 70, no. 1, pp. 655–665, Jun. 2021.
- [6] S. Chae, S. Oh, and S. Park, "Analysis of mutual coupling, correlations, and TARC in WiBro MIMO array antenna," *IEEE Antennas Wireless Propag. Lett.*, vol. 6, pp. 122–125, 2007.
- [7] D. M. Pozar, "A relation between the active input impedance and the active element pattern of a phased array," *IEEE Trans. Antennas Propag.*, vol. 51, no. 9, pp. 2486–2489, Sep. 2003.
- [8] Y. Wu, J. W. M. Bergmans, and S. Attallah, "Effects of antenna correlation and mutual coupling on the carrier frequency offset estimation in MIMO systems," in *Proc. Int. Conf. Wireless Commun. Netw. Mobile Comput. (WiCOM)*, Chengdu, China, Sep. 2010, pp. 1–4.
- [9] S. Lui and H. T. Hui, "Mutual coupling compensation for direction finding using receiving mutual impedance," *Proc. Int. Symp. Antennas and Propag. Conf. Proc.*, Kaohsiung, Taiwan, 2014, pp. 61–62.
- [10] B. K. Lau, J. B. Andersen, G. Kristensson, and A. F. Molisch, "Impact of matching network on bandwidth of compact antenna arrays," *IEEE Trans. Antennas Propag.*, vol. 54, no. 11, pp. 3225–3238, Nov. 2006.
- [11] Z. Ying and D. Zhang, "Study of the mutual coupling, correlations and efficiency of two PIFA antennas on a small ground plane," *IEEE Antennas Propag. Soc. Int. Symp.*, Washington, DC, USA, Jul. 2005, pp. 305–308.
- [12] X. Chen, S. Zhang, and A. Zhang, "On MIMO-UFMC in the presence of phase noise and antenna mutual coupling," *Radio Sci.*, vol. 52, no. 11, pp. 1386–1394, 2017.
- [13] K. H. Chen and J. F. Kiang, "Effect of mutual coupling on the channel capacity of MIMO systems," *IEEE Trans. Veh. Technol.*, vol. 65, no. 1, pp. 398–403, Jan. 2016.
- [14] R. Janaswamy, "Effect of element mutual coupling on the capacity of fixed length linear arrays," *IEEE Antennas Wireless Propag. Lett.*, vol. 1, pp. 157–160, 2002.
- [15] L. Savy and M. Lesturgie, "Coupling effects in MIMO phased array," in *Proc. IEEE Radar Conf. (RadarConf)*, Philadelphia, PA, USA, May 2016, pp. 1–6.
- [16] M. Afaque Azam, A. Kumar Dutta, and A. Mukherjee, "Performance analysis of dipole antenna based planar arrays with mutual coupling and antenna position error in mm wave hybrid system," *IEEE Trans. Veh. Technol.*, vol. 70, no. 10, pp. 10209–10221, Oct. 2021.
- [17] C. Fager, X. Bland, K. Hausmair, J. C. Cahuana, and T. Eriksson, "Prediction of smart antenna transmitter characteristics using a new behavioral mode ling approach," in *Proc. IEEE MTT-SInt. Microw. Symp. Dig.*, Tampa, FL, USA, Jun. 2014, pp. 1–4.
- [18] X.-J. Zou, G.-M. Wang, Y.-W. Wang, and H.-P. Li, "An efficient decoupling network between feeding points for multielement linear arrays," *IEEE Trans. Antennas Propag.*, vol. 67, no. 5, pp. 3101–3108, May. 2019.
- [19] M. Li, Y. Zhang, D. Wu, K. L. Yeung, L. Jiang, and R. Murch, "Decoupling and matching network for dual-band MIMO antennas," *IEEE Trans. Antennas Propag.*, vol. 70, no. 3, pp. 1764–1775, Mar. 2022.
- [20] D. Gao, Z. Cao, S. Fu, X. Quan, and P. Chen, "A novel slot-array defected ground structure for decoupling microstrip antenna array," *IEEE Trans. Antennas Propag.*, vol. 68, no. 10, pp. 7027–7038, Oct. 2020.
- [21] X. Yang, Y. Liu, Y. Xu, and S. Gong, "Isolation enhancement in patch antenna array with fractal UC-EBG structure and cross slot," *IEEE Antennas Wireless Propag. Lett.*, vol. 16, pp. 2175–2178, 2017.
- [22] Z. Qamar, U. Naeem, S. A. Khan, M. Chongcheawchamnan, and M. F. Shafique, "Mutual coupling reduction for high-performance densely packed patch antenna arrays on finite substrate," *IEEE Trans. Antennas Propag.*, vol. 64, no. 5, pp. 1653–1660, May. 2016.
- [23] M. Li and S. Cheung, "A novel calculation-based parasitic decoupling technique for increasing isolation in multiple-element MIMO antenna arrays," *IEEE Trans. Veh. Technol.*, vol. 70, no. 1, pp. 446–458, Jan. 2021.
- [24] W. Yang, L. Chen, S. Pan, W. Che, and Q. Xue, "Novel decoupling method based on coupling energy cancellation and its application in 5G dual-polarized high-isolation antenna array," *IEEE Trans. Antennas Propag.*, vol. 70, no. 4, pp. 2686–2697, Apr. 2022.
- [25] Z. Wang, L. Zhao, Y. Cai, S. Zheng, and Y. Yin, "A meta-surface antenna array decoupling (MAAD) method for mutual coupling reduction in a MIMO antenna system," *Sci. Rep.*, vol. 8, Feb. 2018, Art. no. 3152.
- [26] M. Li, B. Zhong, and S. W. Cheung, "Isolation enhancement for MIMO patch antennas using near-field resonators as coupling-mode transducers," *IEEE Trans. Antennas Propag.*, vol. 67, no. 2, pp. 755–764, Feb. 2019.
- [27] S. Luo, P. Mei, Y. Zhang, G. F. Pedersen, and S. Zhang, "Decoupling of dual-polarized antenna arrays using non-resonant metasurface," *IEEE Trans. Circuits Syst. II, Exp. Briefs*, submitted for publication.
- [28] Y. Zhang, S. Zhang, J. Li, and G. F. Pedersen, "A transmission-line-based decoupling method for MIMO antenna arrays," *IEEE Trans. Antennas Propag.*, vol. 67, no. 5, pp. 3117–3131, May 2019.
- [29] S. Zhang, X. Chen, and G. F. Pedersen, "Mutual coupling suppression with decoupling ground for massive MIMO antenna arrays," *IEEE Trans. Veh. Technol.*, vol. 68, no. 8, pp. 7273–7282, Aug. 2019.
- [30] K. Wu, C. Wei, X. Mei, and Z. Zhang, "Array-antenna decoupling surface," *IEEE Trans. Antennas Propag.*, vol. 65, no. 12, pp. 6728–6738, Dec. 2017.
- [31] C. Wei, Z. Zhang, and K. Wu, "Phase compensation for decoupling of large-scale staggered dual-polarized dipole array antennas," *IEEE Trans. Antennas Propag.*, vol. 68, no. 4, pp. 2822–2831, Apr. 2020.
- [32] P. Mei, Y. Zhang, and S. Zhang, "Decoupling of a wideband dual-polarized large-scale antenna array with dielectric stubs," *IEEE Trans. Veh. Technol.*, vol. 70, no. 8, pp. 7363–7374, Aug. 2021.



**SHENGYUAN LUO** received the B.E. and M.S. degrees from Harbin Engineering University in 2015 and 2019, respectively. He is currently working with Aalborg University, Denmark. His recent research interests include microstrip antennas, wideband antennas, millimeter-wave array antennas, and massive MIMO antenna arrays.



**YIMING ZHANG** (Member, IEEE) received the B.S. degree from Central China Normal University in 2008, and the M.S. and Ph.D. degrees from the University of Electronic Science and Technology of China in 2014 and 2019, respectively. He was a Postdoctoral Researcher with the Antenna, Propagation and Millimeter-Wave Systems Section, Aalborg University, Denmark. His current research interests include MIMO antenna decoupling, single-channel full-duplex communications, and passive RF and microwave components.



**GERT FRØLUND PEDERSEN** (Senior Member, IEEE) was born in 1965. He received the B.Sc. and E.E. (Hons.) degrees in electrical engineering from the College of Technology, Dublin Institute of Technology, Dublin, Ireland, in 1991, and the M.Sc.E.E. and Ph.D. degrees from Aalborg University, Aalborg, Denmark, in 1993 and 2003, respectively. He was a Consultant for the development of more than 100 antennas for mobile terminals, including the first internal antenna for mobile phones in 1994 with lowest SAR, first

internal triple-band antenna in 1998 with low SAR and high TRP and TIS, and lately various multiantenna systems rated as the most efficient on the market. He has worked most of the time with joint university and industry projects and has received more than U.S. \$21 million in direct research funding. He has been one of the pioneers in establishing over-the-air measurement systems. The measurement technique is now well established for mobile terminals with single antennas. Since 1993, he has been with Aalborg University, where he is currently a Full Professor with the Antennas, Propagation and Millimeter-wave Systems Laboratory with 25 researchers and the Head of the Doctoral School on Wireless Communication with 40 Ph.D. students enrolled. He is the Project Leader of the RANGE Project with a total budget of over U.S. \$8 million investigating high-performance centimeter/millimeter-wave antennas for 5G mobile phones. He is currently involved in multiple-input and multiple-output (MIMO) OTA measurement. He has authored over 500 peer-reviewed papers, six books, and 12 book chapters, and holds over 50 patents. His current research interests include radio communication for mobile terminals, especially small antennas, diversity systems, propagation, and biological effects. He has chaired various COST groups with liaison to 3GPP and CTIA for over-the-air test of MIMO terminals.



**SHUAI ZHANG** (Senior Member, IEEE) received the B.E. degree from the University of Electronic Science and Technology of China, Chengdu, China, in 2007, and the Ph.D. degree in electromagnetic engineering from the Royal Institute of Technology, Stockholm, Sweden, in 2013, where he was a Research Fellow. In April 2014, he joined Aalborg University, Denmark, where he currently works as an Associate Professor. From 2010 to 2011, he was a Visiting Researcher with Lund University, Sweden, and Sony Mobile

Communications AB, Sweden. He was also an External Antenna Specialist with Bang & Olufsen, Denmark, from 2016 to 2017. He has coauthored over 80 articles in well-reputed international journals and over 16 (U.S. or WO) patents. His current research interests include mobile terminal mm-wave antennas, biological effects, CubeSat antennas, massive MIMO antenna arrays, UWB wind turbine blade deflection sensing, and RFID antennas.